+++**rapid research letters** +++

pss

www.pss-rapid.com

Plasmonic tuning of aluminum doped zinc oxide nanostructures by atomic layer deposition

Conor T. Riley[1], **Tien A. Kieu**[1], **Joseph S. T. Smalley**[2], **Si Hui Athena Pan**[2], **Sung Joo Kim**[3],
Kirk W. Post[4], **Alireza Kargar**[4], **Dimitri N. Basov**[4], **Xiaoqing Pan**[3], **Yeshaiahu Fainman**[2,5],
Deli Wang[*,2,5], **and Donald J. Sirbuly**[**,1,5]

[1] Department of NanoEngineering, University of California, San Diego, La Jolla, CA 92093, USA
[2] Department of Electrical and Computer Engineering, University of California, San Diego, La Jolla, CA 92093, USA
[3] Department of Materials Science and Engineering, University of Michigan, Ann Arbor, Michigan 48109, USA
[4] Department of Physics, University of California, San Diego, La Jolla, CA 92093, USA
[5] Materials Science and Engineering, University of California, San Diego, La Jolla, CA 92093, USA

[*] Corresponding author: e-mail deliwang@eng.ucsd.edu,
[**] e-mail dsirbuly@ucsd.edu

Currently there is a strong interest in plasmonic materials operating in the near-infrared (NIR), however, conventional metals such as gold and silver possess high optical losses in this region. In this work we demonstrate localized surface plasmon resonances (LSPRs) with low loss in the NIR region by utilizing atomic layer deposition to deposit thin films of aluminium doped zinc oxide onto silicon nanopillars created via nanopshere lithography. The deposited films have excellent conformality and the LSPRs can be tuned from the mid-infrared to the NIR by controlling the doping concentration, deposition temperature and nanostructure morphology.

1 Introduction The field of plasmonics has grown at an aggressive pace over the past century, fueled mainly by a host of exciting applications, including new optical interconnects [1], cancer therapeutics [2], biosensors [3], spectroscopy [4], enhanced energy conversion schemes [5], light emission [6], and novel light–matter interaction (e.g., metamaterials) [7]. Most plasmonic materials consist of noble metals such as gold or silver due to their strong resonances in the visible part of the electromagnetic spectrum. However, noble metals pose an immediate problem for many plasmonic devices since they are expensive, possess high loss at near infrared (NIR) wavelengths and are not well-suited for complementary metal–oxide–semiconductor (CMOS) processing. An alternative approach is to use highly doped semiconductors which have tunable plasmon resonances in the NIR to mid-IR region (0.8–3 μm) [8].

In order to be a viable candidate for many plasmonic applications a semiconductor should fulfill two criteria: (1) a carrier density large enough to display reso-nances in the infrared ($>10^{20}$ cm^{-3}) and (2) low optical losses at resonant frequencies (i.e., be spectrally isolated from inter- and intraband transitions). Taking these criteria into account, the materials to be considered include silicon [9, 10], germanium [11], III–V compound semiconductors (e.g., GaAs, InP, GaN) [12–15], and transparent metal oxides (e.g., ZnO, indium tin oxide) [16, 17]. Of these materials aluminum doped zinc oxide (AZO) is a leading candidate since it has shown the lowest loss for materials operating at NIR wavelengths [18, 19]. Moreover, AZO is a visibly transparent conducting oxide that can be deposited by many facile methods common to the modern semiconductor industry such as RF magnetron sputtering [20], pulsed laser deposition [19], and atomic layer deposition (ALD) [21–23] ALD is a gas phase deposition process that requires self-limiting, sequential surface reactions [24]. This highly controllable surface chemistry has earned ALD considerable attention from the semiconductor industry due to its unmatched ability to create smooth, pinhole free,

tunable, and ultra-conformal films with thickness control on the angstrom scale. Despite these highly advantageous characteristics, no studies displaying tunable localized surface plasmonics via ALD have been demonstrated to the best of our knowledge.

Many of the plasmonic-based applications listed earlier require nanostructured morphologies to enhance light-matter interactions. One approach to creating nanostructures is to etch the structures directly into the material of interest. However, for AZO this is difficult since the anisotropic etching required to make high aspect ratio and multifaceted structures is not well studied and extremely challenging. There have been some advances in bottom-up approaches [25] but achieving well-aligned nanostructures with controlled morphology has not yet been realized. An alternate approach is to coat thin films on substrates that can be easily etched, have well-characterized properties, and are transparent at the desired optical frequencies. Silicon meets these criteria and great success has been made in synthesizing well-controlled nanostructures from techniques such as electron beam [26], nanoimprint [27] and nanosphere lithography (NSL) [28]. NSL can provide a simple route to create high aspect ratio nanostructures on large area silicon substrates at a fraction of the time and cost of electron beam lithography, allowing for the investigation of many different parameters in a short time span. For these reasons, we utilized NSL to fabricate silicon nanopillar (SiNP) arrays and made them plasmonically active by coating with thin ($\sim$50 nm thick) AZO films deposited via ALD. By controlling the dimensions of the silicon templates, AZO doping concentrations, and deposition conditions we demonstrate highly tunable LSPRs in the IR frequency range.

2 Experimental NSL was carried out using an adapted process from Hsu et al. [28] Briefly, silica particles were synthesized using the Stöber process [29] and functionalized with aminopropyl-methyldiethoxysilane (APMDES) and transferred to a close-packed geometry with a Langmuir–Blodgett trough (KSV NIMA). The diameters of the silica spheres were reduced using reactive ion etching (Oxford P80 RIE) with a gas concentration of $1:1$ Ar$:$CHF$_3$. To fabricate the nanopillars the unmasked silicon was etched with an Oxford P100 RIE-ICP using a gas concentration of $1:2$ SF$_6:$C$_4$F$_8$. The remaining silica mask was then removed by immersing the substrate in a $6:1$ buffered oxide etch (BOE). AZO films were deposited on the silicon nanopillar templates via ALD using a Beneq TFS200 atomic layer deposition system where the zinc, aluminum and oxygen sources were diethylzinc (DEZ), trimethylaluminum (TMA) and water, respectively. The films were grown by applying either a zinc or aluminum cycle before a water cycle at temperatures spanning from 200 °C to 250 °C. The aluminum concentration was controlled by changing the frequency of the TMA precursor cycle. For example, a film of $\sim$2 wt% Al/Zn (nominal) was synthesized by using 1 TMA cycle for every 20 DEZ cycles.

All AZO film thicknesses were quantified on planar silicon substrates via ellipsometry using a filmetrics F20. Optical measurements were carried out on the AZO nanopillar arrays using a Perkin Elmer Lambda 1050. Hall measurements were performed on a home-built set-up using the van der Pauw method at room temperature with a magnetic field of 3000–5000 G. Nanostructure imaging was carried out using an FEI XL30 ultrahigh resolution SEM. The atomic-scale structural analyses were carried out using a high-resolution transmission electron microscopy (HRTEM, JEOL JEM3100F) operating at 300 kV. Ellipsometry measurements were carried out using a commercial Woolam VASE ellipsometer that scanned from 300 nm to 2000 nm on a 90 nm thick AZO films ($1:15$ Al$_2$O$_3:$ZnO cycle ratio) deposited at 250 °C. The remaining optical constants from 2000 nm–3000 nm were extrapolated from the ellipsometry data using the Lorentz–Drude model (see Supporting Information (SI), Table S1). XRD patterns were taken with a Rigaku Rotaflex using the Cu K$_\alpha$ wavelength.

FDTD simulations were carried out using Lumerical. Periodic boundary conditions were employed with a plane wave 9.3 fs pulse at normal incidence with broadband excitation of 1400 nm to 3000 nm. The silicon nanopillars were designed with similar dimensions to the experimental results ($D = 200$ nm, $L = 540$ nm) and coated with a 50 nm AZO film. The AZO film was modeled using the dielectric constants acquired from ellipsometry.

3 Results and discussion The AZO coatings were created by depositing one Al$_2$O$_3$ cycle for every 15–30 ZnO cycles at 200–250 °C onto either planar substrates or the SiNPs created by NSL. Unless specified otherwise, SiNPs with $\sim$200 nm diameters, 540 nm lengths and a 480 nm pitch were used. These dimensions were chosen to be small enough to eliminate any photonic modes in the SiNP [30] yet large enough to create well defined SiNPs. A representative array of SiNPs is shown in Fig. 1a, b. The cross-sectional image in Fig. 1c of a larger SiNP (to allow easier cleavage for imaging) shows that the AZO coatings are highly conformal, whereas the high-resolution transmission electron micrograph (Fig. 1d) reveals the AZO crystal structure with a lattice spacing of 0.26 nm corresponding to the (001) plane of the wurtzite crystal structure. Further confirmation of the AZO films comes from X-ray diffraction (Fig. 1e) which shows peaks (for a $1:20$ Al$_2$O$_3:$ZnO cycle ratio AZO coating) that correspond to wurtzite ZnO. Importantly, there is no evidence of crystalline impurities such as Al$_2$O$_3$ or ZnAl$_2$O$_4$. Additional XRD runs were carried out on planar AZO films synthesized at 200 °C with $1:15$–$1:30$ Al$_2$O$_3:$ZnO deposition cycle ratios to monitor any variations in the diffraction peaks as the Al incorporation was altered (see SI, Figs. S1–S3). As the Al cycle frequency increases, all of the wurtzite diffraction peaks shift to higher angles. Since the ionic radius of Al^{3+} is considerably smaller (0.53 Å) than Zn^{2+} (0.74 Å), a decrease in the d-spacing between atomic planes is expected
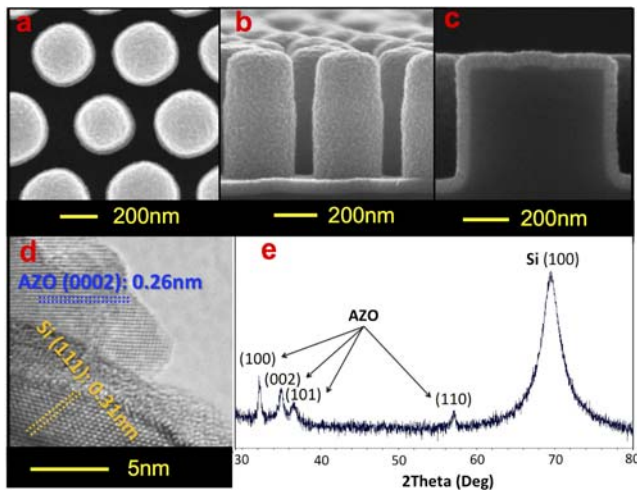
Figure 1 SEM image of (a) the top and (b) cross-section of a representative AZO-coated SiNP array ($D = 303$ nm). (c) HRTEM image of an ALD-deposited AZO layer. The AZO is being imaged from an area that peeled away from the nanopillar during cleavage of the silicon substrate. (d) Cross-sectional image of a larger diameter ($D = 662$ nm) AZO-coated SiNP showing a highly conformal film deposited by the ALD process. (e) XRD pattern of a planar silicon wafer coated with an AZO film deposited with a $1:20$ $Al_2O_3:ZnO$ cycle ratio at 200 °C.

to occur when Zn sites are substituted by Al atoms. When the Al cycle frequency is kept constant at $1:15$, and the temperature is increased from 200 °C to 275 °C, similar shifts to higher angles are also seen. This can be explained by higher incorporation of Al at elevated temperatures or by an increase in oxygen vacancies which has been observed in ZnO films deposited by ALD [31].

To further investigate the effect of Al doping on the carrier concentration, we performed Hall measurements on 50 nm ALD films prepared under different conditions. We found that by increasing the Al cycle occurrence from $1:30$ to $1:15$ $Al_2O_3:ZnO$ the carrier concentration increased linearly from 1.5×10^{20} to 3.6×10^{20} cm^{-3} (see SI, Fig. S4). At cycle ratios above $1:15$, and a growth temperature of 200 °C, there were no further increases observed in the carrier concentration indicating that an upper limit on Al doping had been achieved. Above this concentration AlO_x suboxide clusters may form, creating an insulating character within the film which leads to a decreased carrier concentration [32]. When keeping the deposition temperature constant and increasing the aluminium cycle frequency, the hall mobility drops and the carrier concentration increases. The decrease in mobility is expected due to an increase in electron-impurity scattering. By increasing the temperature from 200 °C to 250 °C, and holding the Al cycle ratio constant at $1:15$, the carrier concentration can be further increased from 3.6×10^{20} to 9.3×10^{20} cm^{-3} (see SI, Fig. S4). All of the hall measurements support the XRD data which show similar trends (i.e., higher conductivity, smaller d-spacing) when the carrier concentration is increased. This is strong evidence that
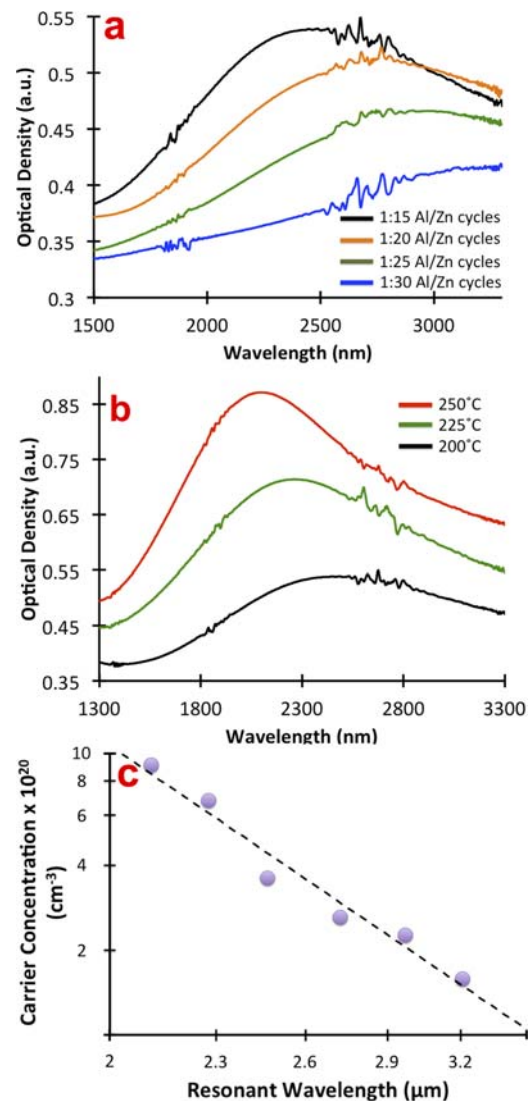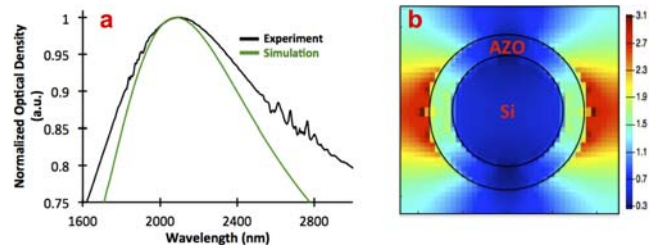

Figure 2 IR extinction spectra of AZO-coated SiNPs deposited at (a) constant temperature (200 °C) and varying Al/Zn compositions and (b) constant Al/Zn composition ($1:20$ $Al_2O_3:ZnO$ cycle ratio) at different deposition temperatures. (c) Log–log plot of carrier concentration vs. resonant wavelength for various AZO-coated SiNP arrays showing a linear relationship (dashed line) in accordance with the Drude model. Here, the resonant wavelength is defined as the wavelength at peak optical density.

the substitution of Al into the ZnO lattice is not only causing changes in the crystal lattice parameters but also significantly altering the electronic properties of the material.

Extinction spectra of 50 nm AZO-coated SiNPs are shown in Fig. 2a and b. The spectra have well defined LSPR bands which can be tuned by changing the Al/Zn cycling ratios and/or growth temperature. Bare SiNP arrays and undoped ZnO-coated SiNP arrays were also carried out as controls which showed no optical responses at these frequencies (see SI, Fig. S5). Furthermore, a coated SiNP ($1:15$ $Al_2O_3:ZnO$) was deposited at 200 °C and annealed

for 1 hour at 250 °C in the reactor chamber resulting in no significant change to the optical or electrical properties. This indicates that the doping occurs as a result of the ALD crystal growth, and temperature dependent sticking coefficients of the source chemicals, as opposed to temperature activation of the dopants [24]. The blue shift in the LSPR frequency, ω_{LSPR}, from 3200 nm to 2100 nm as the carrier concentration is increased is predicted by the Drude model [33] which can be expressed as $\omega_{LSPR} \propto \omega_p = (n\,e^2/m_e\varepsilon_0)^{1/2}$ where ω_p is the bulk plasmonic frequency, n is the carrier concentration, e is the elementary charge, m_e is the effective electron mass, and ε_0 is the vacuum permittivity. The log–log plot in Fig. 2c shows that the LSPRs are tunable from the mid-wavelength IR to the NIR and have a linear relationship that matches well with the Drude model. More importantly the XRD, Hall measurements and spectroscopic data all show that as the aluminum concentration and substrate temperature increase more unbound electrons are added into the wurtzite lattice, blue shifting the plasmonic frequency.

To properly simulate and quantify the LSPR modes we first extracted permittivity values for the AZO layer using ellipsometry. The sample we characterized was deposited at 250 °C with a 1 : 15 Al_2O_3 : ZnO cycle ratio. Optical constants were then determined from the measured ψ and Δ values by modeling the AZO film on silicon using a series of Kramers–Kronig consistent oscillators. The experiments showed a crossover wavelength ($\varepsilon' = 0$, where the material starts to behave like a metal) of 2160 nm with a corresponding imaginary dielectric constant (ε'') of 2 which is directly related to the optical loss of the material (see SI, Fig. S6). Although this loss is considerably lower than noble metals at this wavelength, crossover wavelengths smaller than 1550 nm with lower losses have been reported using PLD [19]. Since our loss values are similar to other ALD studies [23] we believe that the higher loss is due to the lower crystal quality inherent to the ALD deposition process. Furthermore, the optical loss can be shown to be inversely proportional to the electron mobility [8] which often reflects the crystalline quality of a material. Highly doped AZO films deposited by ALD possess mobilities <10 cm^2/V s whereas AZO films created via PLD have been shown to have mobilities as high as 47.6 cm^2/V s [16]. In addition, unlike other thin film deposition methods, it has been shown that the aluminum dopants deposited by ALD maintain their layered configuration which may not be ideal for achieving high carrier concentrations [21]. Although the PLD method has shown better plasmonic properties, the ability of ALD to coat/fill small feature sizes, paramount to the growing field of nano-optics, is still unmatched by any other thin film deposition process. Therefore we believe that it is possible to keep all the synthetic advantages of ALD, while achieving lower losses and negative permittivity at 1550 nm, by increasing the crystallinity and altering the dopant configuration with post-processing steps and/or using substrates with a smaller lattice mismatch.

Figure 3 (a) FDTD simulations showing a comparison of the experimental (black) and simulated (green) extinction spectra for a SiNP ($D = 200$ nm) coated with a 50 nm thick, 1 : 15 Al_2O_3 : ZnO cycle ratio AZO film. (b) Cross-section of an AZO-coated SiNP nanopillar while excited with linearly polarized light at peak resonance (2085 nm).

Next, the obtained optical constants were used in finite-different time-domain (FDTD) simulations on an individual nanostructure with similar dimensions as the experiment (experimental section). The calculated extinction spectrum of the simulated AZO-coated SiNP is shown in Fig. 3a which has a maximum peak at a similar wavelength as the experimental array. The broader experimental peak is mainly attributed to sample inhomogeneities (e.g., lattice disordering, surface roughness), as compared to the perfect simulated array, but inter-pillar coupling could also be contributing to a broader linewidth. A more detailed analysis is required for determining the exact origin of the discrepancies and will be a topic of future work. In these studies it was observed that the predominant LSPR mode at normal incidence is due to the lateral dipole oriented perpendicular to the excitation wavevector with an electric field enhancement factor greater than 3 at the resonant wavelength (Fig. 3b). In addition, a significantly stronger light–matter interaction is observed with increasing incident angle under TM polarization (see SI, Fig. S7) which is a characteristic of the plasmonic modes observed in the simulations [34].

The AZO coating is the only part of the nanostructure that can support a LSPR mode and show a band that is tunable by impurity doping. Therefore, it is expected that additional tuning can be achieved by adjusting the dimensions of the nanostructure array. There was found to be no significant dependence of the LSPR resonant wavelength on the diameter of the SiNPs (see SI, Fig. S8), however, significant red-shifting was observed when the AZO film was increased from 40 nm to 75 nm (see SI, Fig. S9). This indicates that the excited dipole is mainly confined within the AZO shell and not within the silicon core for the dimensions probed. Furthermore, when the inter-pillar distance was decreased, the LSPR broadens and redshifts which is indicative of a plasmonic coupling effect (see SI, Fig. S10).

4 Conclusion In conclusion, we have devised a simple synthetic strategy to fabricate highly tunable, IR-active plasmonic arrays. We demonstrated that NSL could be used to create well-defined, size-selected nanostructures

from nanoparticle masking and gas etching processes. ALD was then utilized to deposit highly-doped AZO thin films. Electrical, optical, and material property measurements were carried out on the AZO-coated nanostructures which all supported the predicted behavior of IR semiconductor plasmonic materials. A Drude theoretical model further validated that the observed shifts in the plasmonic properties arise from the relationship between the plasmon frequency and carrier concentration. With careful adjustments in the deposition conditions, dimensions of the templates, doping concentration, and post-processing techniques, the LSPRs should become tunable from the mid-IR to the important telecommunication wavelength (ca. 1550 nm). This paves the way for new low-loss, highly conformal optical materials that can be used in optoelectronic and telecommunication devices while being fully compatible with modern CMOS processing.

References

[1] D. K. Gramotnev and S. I. Bozhevolnyi, Nature Photon. **4**, 83 (2010).

[2] Y. D. Jin, Acc. Chem. Res. **47**, 1842 (2008).

[3] H. Z. Yu, Y. Li, and L. M. Ou, Acc. Chem. Res. **46**, 258 (2013).

[4] K. L. Wustholz, A. I. Henry, M. McMahon, R. G. Freeman, N. Valley, M. E. Piotti, M. J. Natan, G. C. Schatz, and R. P. Van Duyne, J. Am. Chem. Soc. **132**, 10903 (2010).

[5] H. A. Atwater and A. Polman, Nature Mater. **9**, 205 (2010).

[6] W. Zhou, M. Dridi, J. Y. Suh, C. H. Kim, D. T. Co, M. R. Wasielewski, G. C. Schatz, and T. W. Odom, Nature Nanotechnol. **8**, 506 (2013).

[7] W. Cai and V. Shalaev, Optical Metamaterials: Fundamentals and Applications (Springer Verlag, New York, 2009).

[8] G. V. Naik, V. M. Shalaev, and A. Boltasseva, Adv. Mater. **25**, 3264 (2013).

[9] M. Balkanski, A. Aziza, and E. Amzallag, Phys. Status Solidi **31**, 323 (1969).

[10] R. E. Peale, J. W. Cleary, W. R. Buchwald, and O. Edwards, presented at Biomecial Optics, Miami, FL, USA (2010).

[11] R. Soref and J. W. Hendrickson, Opt. Express **20**, 3814 (2012).

[12] W. Walukiewicz, J. Lagowski, L. Jastrzebski, P. Rava, M. Lichtensteiger, C. H. Gatos, and H. C. Gatos, J. Appl. Phys. **51**, 2659 (1980).

[13] W. Walukiewicz, L. Lagowski, L. Jastrzebski, M. Lichtensteiger, and H. C. Gatos, J. Appl. Phys. **50**, 899 (1979).

[14] T. Yamada, E. Tokumitsu, K. Saito, T. Akatsuka, M. Miyauchi, M. Konagai, and K. Takahashi, J. Cryst. Growth **95**, 145 (1989).

[15] A. Kasic, M. Schubert, S. Einfeldt, D. Hommel, and T. E. Tiwald, Phys. Rev. B **62**, 7365 (2000).

[16] H. Agura, A. Suzuki, T. Matsushita, T. Aoki, and M. Okuda, Thin Solid Films **445**, 263 (2003).

[17] S. Q. Li, P. Guo, Z. Lingxiao, W. Zhou, T. W. Odom, T. Seideman, B. Ketterson, and R. P. H. Chang, ACS Nano **5**, 9161 (2011).

[18] G. V. Naik, J. Kim, and A. Boltasseva, Opt. Mater. Express **1**, 1090 (2011).

[19] J. Kim, G. V. Naik, N. K. Emani, U. Guler, and A. Boltasseva, IEEE J. Sel. Topics Quantum Electron. **19**, 3 (2013).

[20] C. Guillen and J. Herrero, Vacuum **84**, 924 (2010).

[21] D. J. Lee, H. M. Kim, J. Y. Kwon, H. Choi, S. H. Kim, and K. B. Kim, J. Adv. Funct. Mater. **21**, 448 (2011).

[22] S. C. Gong, Y.-J. Choi, H. Kim, C.-S. Park, H.-H. Park, J. G. Jang, H. J. Chang, and G. Y. Yeom, J. Vac. Sci. Technol. A **31**, 01A101 (2013).

[23] A. Frölich and M. Wegener, Opt. Mater. Express **1**, 883 (2011).

[24] S. M. George, Chem. Rev. **110**, 111 (2010).

[25] G. Garcia, R. Buonsanti, E. L. Runnerstrom, R. J. Mendelsberg, A. Llordes, A. Anders, T. J. Richardson, and D. J. Milliron, Nano Lett. **11**, 4415 (2011).

[26] H. J. M. Levinson, M. A. Cerrina Allen, R. D. Skinner, J. G. Neureuther, A. R. Peckerar, M. C Perkins, K. F. Rooks, and M. J., Handbook of Microlithography, Micromachining, and Microfabrication (Society of Photo-Optical Instrumentation Engineers, 1997).

[27] A. Kargar, K. Sun, Y. Jing, C. Choi, H. Jeong, G. Y. Jung, S. Jin, and D. Wang, ACS Nano **7**, 9407 (2013).

[28] C.-M. Hsu, S. T. Connor, M. X. Tang, and Y. Cui, Appl. Phys. Lett. **93**, 133109 (2008).

[29] W. Stöber, A. Fink, and E. Bohn, J. Colloid Interf. Sci. **26**, 62 (1968).

[30] P. Moitra, B. A. Slovick, Z. G. Yu, S. Krishnamurthy, and J. Valentine, Appl. Phys. Lett. **104**, 171102 (2014).

[31] S. Jeon, S. Bang, S. Lee, S. Kwon, W. Jeong, H. Jeon, H. J. Chang, and H.-H. Park, J. Electrochem. Soc. **155**, H738 (2008).

[32] J. G. Lu, S. Fujita, T. Kawaharamura, H. Nishinaka, Y. Kamada, T. Ohshima, Z. Z. Ye, Y. J. Zeng, Y. Z. Zhang, L. P. Zhu, H. P. He, and B. H. Zhao, J. Appl. Phys. **10**, 083705 (2007).

[33] P. Drude, Ann. Phys. **1**, 566 (1900).

[34] S. A. Maier, Plasmonics: Fundamentals and Applications. (Springer, New York, 2007).

Supporting Information Additional Supporting Information may be found in the online version of this article at the publisher's web-site.